A template to obtain information on gravitational mass movements from the spectrograms of the seismic signals generated

Emma Suriñach[1], E.Leticia Flores-Márquez[2]

[1]Department RISKNAT Avalanches Research Group- Institut Geomodels. Dpt. Dinàmica de la Terra i de l'Oceà. Facultat de
5   Ciències de la Terra. c/ Martí i Franquès s/n, Universitat de Barcelona (UB). Barcelona 28008, Spain.
[2]Departamento de Geomagnetismo y Exploración. Instituto de Geofísica, UNAM, Circuito Instituto S/N, Coyoacán 04510,
Mexico,

Correspondence to: Emma Suriñach (emma.surinach@ub.edu)

Abstract. We present a template that helps in the classification of gravitational mass motions (snow avalanches, lahars, and
10   debris flows) by simply overlaying it graphically with the corresponding spectrogram of the generated seismic signal at the
same scale. The template is created with different values of a parameter β' that allows us to analytically reproduce the
exponential form of the increase in amplitude of high frequencies in time of the SON (Signal Onset) section of the
spectrogram when the mass movement descends a slope and approach a seismic sensor. This increasing shape is a
consequence of the appearance of energy at high frequencies as the gravitational mass approaches the seismic sensor. We
15   present a methodology that includes a link between the propagation properties of seismic waves and the results of the
application of an image processing using the Hough transform to demonstrate that this shape is related to the speed of the
avalanche and the characteristics of the terrain. Seismic data generated by lahars, debris flows, and avalanches are used for
the study. Depending on the type of event, differences are obtained in the order of magnitude of the values of β'. The mean
value of β' for lahars is around 0.003 s^{-1}, that for debris flows is an order of magnitude greater (0.017 s^{-1}) and an order of
20   magnitude less than that for avalanches (0.12 s^{-1}). Furthermore, differences in β' are observed within each type of event.
Once the appropriated value of β' has been determined, the characteristics of the mass movement must be set according to
expert judgement. This must be done for each site and for each type of gravitational mass movement. The application of the
templates to the data of lahars and an avalanche recorded in two different places of its trajectory is presented as an example.

1 Introduction

25   The control and knowledge of the behavior of earth surface gravitational mass movements is crucial to reduce their
associated risks. The monitoring of these events helps in the knowledge of hazardous areas basically in twofold: number of
events and areas of occurrence, inputs necessary for hazard assessment, land use planning. Additionally, an understanding of
the characteristics of the mass movement descending a slope enables us to obtain a better control through models and thus,
gain further insight into its evolution. The use of seismic signals generated by mass movements is an emerging field as a

30   method to control these phenomena. This is a non-invasive method that supplies information on the evolution of the phenomena and helps to detect them.

Seismic signals are generated by the friction of the moving mass on the ground, changes in the slope, and by impacts against obstacles (e.g., Dahlen, 1993; Suriñach et al., 2000; Suriñach et al., 2001; Brodsky et al., 2003; Huang et al., 2007; Vilajosana et al., 2007a; Vilajosana et al., 2008; Allstad, 2013). Considering their origin, high frequency seismic signals (f

35   >1Hz) have been used in the lasts decades to model or to characterize the dynamics of the gravitational mass movements (rock falls, landslides, lahars, rock avalanches, submarine slumps,) (e.g. Caplan-Auerbach and Huggel, 2007; Deparis et al., 2008; Zobin et al., 2009; Schneider et al., 2010; Favreau et al., 2010; Lacroix et al., 2012; Allstad, 2013; Dammeier et al., 2015; Hibert et al., 2011, 2015; Lin et al., 2010; Dietze et al., 2017; and Saló et al., 2018). However, one of the problems encountered in these studies to take into account is the dependence of the results on the seismic characteristics of the ground

40   involved (Hibert, et al., 2017). These characteristics affect, inter alia, the calculation of the energy dissipated by the mass movements, which has a repercussion when classifying their size (Suriñach et al., 2018). Kuehnert et al., (2020) studied using SEM simulations the influence of the curvature of the topography in the seismic wave field (wave form and energy amplification) in a specific case at the Dolomieu crater in Piton de la Fournaise Volcano.

Seismic signals have also been employed to localize mass movement events using seismic regional broadband networks as

45   well as local networks installed temporarily. Signal arrival times using array localization methods (beam forming) (e.g., Lacroix and Helmstetter, 2011; Hibert et al., 2017), classic earthquake localization methods, and travel time seismic profiles approaches (e.g., van Herwijnen and Schweizer (2011a and 2011b); Manconi et al., 2016; Moore et al., 2017; Spillmann et al., 2007; Zimmer et al., 2012 and Zimmer and Sitar, 2015) have been used to localize these events. In Allstadt et al., (2018) a revision of the state of the art of the use concerning seismic signals related to mass movements associated to volcanoes can

50   be found. Part of the issues presented can be extrapolated to other mass movements. Recently, ASL (spectral amplitude) methods have also been used to localize snow avalanches (Pérez-Guillén et al., 2019) and one landslide in Japan (Doi and Maeda, 2020). In all these studies, basically, the time series and the signals of more than one sensor were used.

As regards debris flows, was Arattano (1999) who firstly used seismic detectors to monitor debris flows. Later, seismic signals have also been used to analyze debris flow using algorithms based on duration/intensity threshold (e.g., Arattano and

55   Marchi, 2005; Abancó et al., 2014; Schimmel & Hübl, 2015). More recently, Coviello et al., (2019) using a linear array of geophones installed along a channel developed an algorithm based on the signal intensity STA / LTA ratio (from short to long term), to obtain information on the discharge of the flow and, therefore, the estimation of the magnitude and duration of the event, useful to warning purposes. Moreover, hyperconcentrated flows properties were inferred from the peaks of frequency and the amplitudes of the signals recorded by a geophone installed outside the channel (Coviello et al., 2018).

60   The use of the signal frequency content is not as widespread as that of the time series amplitude. In addition of the use of the time series (seismograms), their spectrum (i.e., PSD) is also used. In the spectrum is represented the all the frequency content of a portion of a signal or the entire signal. The frequency content of the signals has been included in the process of classification of events using HHM (Hidden Markov Models) using more than one sensor (e.g., Dammeier et al., 2015 and

Dammeier et al., 2016). The information on the evolution of the frequency in time is lost in the spectrum. Spectrograms or
65 running spectrum (also sonograms) constitute another representation of the signal in the frequency-time domain to study the
characteristics of the seismic signals considering their frequency content evolution. This is a visual representation of the
matrices of the amplitude values of the spectra of a temporal signal calculated in consecutive time windows. For the sake of
brevity, the word "spectrogram" will replace the sentence "spectrogram of the seismic signals generated by a mass
movement", hereafter.

70 In most of the studies the spectrograms have been used as complementary information of the time signals, basically to
discern among different processes that generate a seismic wave field (earthquakes, helicopters, planes, gravitational mass
movements, etc.…). Cole et al., 2009 and Kostantinous et al., 2021 (lahars), van Herwijnen and Schweizer, 2011a (snow
avalanches), Burtin et al., 2016 (torrential and fluvial processes), Walter et al., 2017 (debris flows) and Feng et al., 2017 or
Doi and Maeda, 2020 (landslides) are some examples.

75 Different algorithms calculate the spectrograms. Moreover, several computer libraries include the algorithm for the
spectrogram function in different programming languages (e.g., Matlab®, Python etc.). The spectrograms we used were
calculated by algorithms developed by our group. This allows greater control of the parameters and values obtained and their
representation.

Our analysis of hundreds of spectrograms seismic signals generated by different snow avalanches indicated a connection
80 between the type and evolution of the snow avalanches and the shape of the spectrograms (Biescas et al., 2003; Biescas,
2004; Vilajosana et al., 2007a; Vilajosana, 2008; Vilajosana et al., 2008 and Pérez-Guillén et al., 2016). Recently, we
presented a method to estimate the evolution of an avalanche along a path at Vallée de la Sionne (VdLS) experimental site
based on the spectrograms of the generated seismic signals recorded in sensors, each one placed at a different location along
the path (Suriñach et al., 2020). Particularly, we used the initial section of the spectrograms corresponding to avalanches that
85 approach a sensor. This section is named SON (Signal Onset) whereas the section corresponding when the avalanche passes
over o near the sensor is named SBO (Signal Body) as defined by Roig-Lafon (2021) and references therein.

We focus our attention on the spectrogram SON section, where the increase in the amplitudes of the high-frequency content
over time presents a slope that increases exponentially as the avalanche approaches the seismic sensor, when the amplitudes
are displayed on a logarithmic scale (e.g., Fig. 1b). This increasing of amplitudes according to the frequency is due to the
90 effect of the attenuation of the seismic waves in a medium because the anelastic/intrinsic attenuation and the geometrical
spreading (e.g., Aki and Richards, 1980; Lay and Wallace, 1995), and to the fact that the avalanche approaches the sensor.
This increase has already been observed by Leprêttre et al., (1996) and Kishimura and Izumi (1997). Biescas et al., (2003)
highlighted this increase in amplitudes in the avalanche spectrograms for the first time.
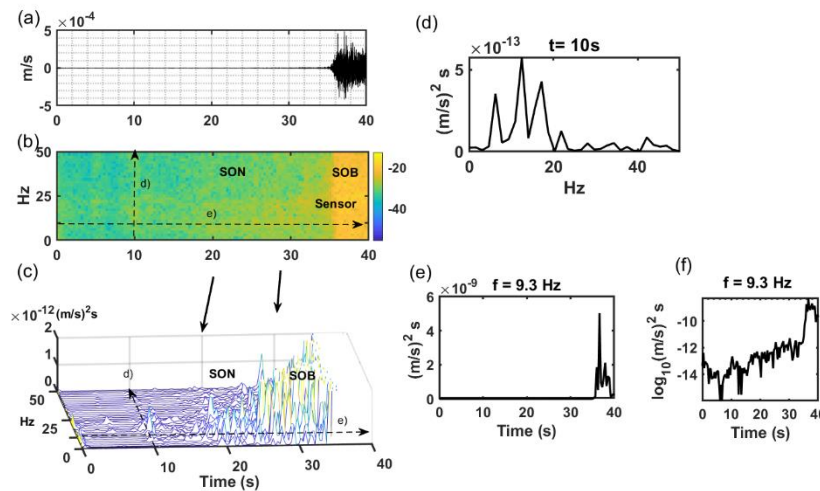
95 **Figure 1. a) time series (seismogram) recorded from a mass movement. Two representations of the frequency content of the time series: b) Spectrogram of the time series. The amplitude values ((m s^{-1})^2 s) are in log$_{10}$ escale. c) Image representation in the waterfall form of the amplitudes. SON and SOB sections are indicated. Time (s) in horizontal axes. d) Amplitude frequencies transect for t = 10 s indicated as d) in b) and c). e) Amplitude (m s^{-1})^2 s frequencies transect for f= 9.3 s indicated as e) in b) and c) and f) Amplitude (m s^{-1})^{2}s frequency transect for f= 9.3 s in logarithmic scale indicated as e) in b) and c).**

100

This increase in amplitudes with increasing frequency is also present in other spectrograms of moving seismic energy sources that approach a sensor such as vehicles (e.g., Almendros et al., 2002; Anderson et al., 2004; Ketcham et al., 2005; Moran and Greenfield, 2008) and trains (Fuchs et al., 2018; Lavoué et al., 2021). Natural phenomena as volcanoes and other gravitational mass movements (e.g., Allstadt et al., 2018) and meteotsunamis (Okal, 2021) also show this behavior.

105 However, in all these cases the information used from the spectrograms was minor, only considered as complementary visual information.

In earlier studies that used the information contained in the spectrograms we have found similarities in the characteristics of the spectrograms generated by the snow avalanches and those associated with other gravitational mass movements, (landslides: Suriñach et al., 2005; debris flows: Kogelnig et al., 2014; lahars: Vázquez et al., 2016).

110 The method presented allows us to obtain quantitative information from the spectrograms of the SON section seismic signals generated by gravitational mass movements descending a slope and approaching a seismic sensor. This quantification allows us to obtain two parameters that can analytically reproduce the increasing shape of amplitude according to the frequency of the SON section. Because this shape is related to the avalanche speed and to the characteristics of the terrain, the two parameters allow us "to classify" the mass movement. Note that this crescent shape is not affected by the size of the

115 avalanche, as this affects all frequencies simultaneously.

To obtain these parameters we regarded the spectrogram as an image, and by applying image processing, we obtain parameters that define the increasing shape of the spectrogram. To this end, the spectrograms were prepared for the application of the Hough Transform (HT). The HT is regarded as a discretization of the Radon transform (Hough, 1962), defined as an integral over a line. It is applied as a generalization to detect arbitrary non-regular forms of objects. The shapes

120 can be delineated either by a set of known functions (circles, ellipses, curve segments, hyperbolas) or by means of templates, previously designed, that consider the shape of the object (van Ginkel et al., 2004). In particular, when the border to detect is a straight line, its application has proved been very useful in many fields, for instance to a) detect geological faults from seismic sections (AlBinHassan and Marfurt, 2003), b) enhance geological structures from two-dimensional image-profiles constructed from ground-penetrating radar (Rivera-Ríos and Flores-Márquez, 2012), and c) develop face recognition

125 software (Varun et al., 2015). To obtain quantitative information from the SON section of the spectrograms, several codes and computer functions were developed in Matlab® code. This method consists of several steps that include numerical calculations developed specifically for this work, including the algorithm to calculate the spectrogram.

The paper is divided in eight sections: after this introduction a description of the data used with a briefly explanation of the post-acquisition treatment of the recorded signals constitutes Sect. 2. In Sect. 3 the methodology is presented. This section

130 includes the differences between a spectrogram and a spectrum of a signal and the interpretation of the shape of the spectrogram in terms of the SON section. Sect. 4 is devoted to the fundamental methodology of the spectrogram treatment. In Sect. 5, the results of the application of the method to different signals generated by different gravitational mass movements (lahars, debris flows, and snow avalanches of two different sites) are presented. Sect. 6 is devoted to the discussion. In Sect. 7, a template created with the two parameters useful for classifying the events is presented and applied to

135 different examples. The conclusions constitute Sect. 8.

2 Characteristics of the data used

This study utilizes data obtained in different experimental sites and of different gravitational mass movement. a) snow avalanches recorded at the VdlS test site (SLF, Switzerland) and Ryggfonn experimental site (NGI, Norway), b) lahars

140 recorded at the Colima Volcano, (CUEIV and UNAM, México), and c) debris flow recorded at Lattenbach catchment (BOKU, Austria). In this study different seismic recording stations were used to obtain the seismic data, depending on the case. Given that data depend on the characteristics of the recording stations (site and sensor), data acquisition system parameters and post-acquisition treatment, a control of the data used is important because this conditions the results and their interpretation. Data of snow avalanches were obtained in stations consisting of a three-component seismometer Mark L-4C-

145 3D (Mark Products) of eigenfrequency 1 Hz and a data acquisition system Reftek–130 (Trimble). The characteristics of the recording stations at VdlS test site are indicated in Sovilla et al., (2013) and Pérez-Guillén et al., (2016). In the present contribution we considered the data obtained only in cavern B placed at 985 m distance from the crown (CB1) (see Fig. 10). The characteristics of the recording stations at the Ryggfonn experimental site, similar to those of VdlS, are indicated in

Vilajosana et al., (2007a) and Vilajosana et al., (2007b). In this case we considered the data recorded at station in the track,
150   placed approx. at 1450 m from the crown (see Fig. 12, TR). The recording station characteristics for the lahars of the Colima
Volcano, México (see Fig. 6) are described in Capra et al., (2018) and references therein. Data were recorded in a Guralp
CMG-6TD broadband seismometer (0.03–100 Hz of frequency range), installed ~100 m away the main channel of the
Montegrande ravine at ~2100 m.a.s.l. The complete characteristics of the recording station of the debris flow placed at
Lattenbach catchment (Austria) are indicated in Kogelnig et al., (2014) (see Fig. 8). The geophone was a SM4 with a
155   frequency range of 10-180 Hz and a sensitivity of 28.8 V/m/s placed on land beside the channel of the flux at a very short
distance (<10 m). In addition to the seismic signals generated by the debris flow, infrasound data were also obtained with a
nearby microphone 'Gefell WME 960H' with a 0.5 Hz–20 kHz frequency range and 50 mV Pa^{-1}. The two types of
measurements were obtained time synchronized with the aim to compare the suitability and sensitivity of the two types of
instruments for monitoring purposes. All seismic and infrasound data, collected at 100/200 s.p.s. (50/100) Hz Nyquist
160   frequency) were transformed into ground velocity (m s^{-1}) or pressure (Pa), respectively using the conversion factors indicated
by the manufacturers. In all the cases studied, the flux of mass (snow, lahar, debris) passed over or laterally very close the
seismic sensors that were installed oriented orthogonal to the vertical direction and in the N-S and E-W directions.

2.1 Post-acquisition treatment of the seismic signal

All seismic signals were band-pass filtered [1-40] Hz with a 4th- order Butterworth filter. Avalanche seismic data were
165   analyzed considering only one seismogram named final seismogram (FS). To construct this single vector seismogram from
the 3 seismic components (Z, N-S, E-W), that maintains all the seismograms characteristics, the vector properties in the 3D
space were considered. Only the vector amplitude was considered in the spectrogram. The construction process is explained
in Suriñach et al., (2020). The seismograms of vertical component were used for lahars and debris flows. As mentioned, only
the SON section of the spectrogram was considered in the study. In the calculation, the short-time FFT with a Hanning
170   window (length 0.64 s/1.28 s) and 50% of overlap (0.32 s/0.64 s) was used according to the sample rate. The length and
overlap of the time windows for the spectrograms were fixed according to the time series characteristics. The resolution in
frequencies is 0.0156 Hz/0.0078 Hz and the resolution in time is 0.32 s/0.64 s, according to the sample rate.

3 Spectrogram vs spectrum

Bellow some points regarding the characteristics of the spectrogram vs. spectrum because their understanding is fundamental
175   for our purpose. The evolution in time of the frequency content of a time series usually is represented by the spectrogram. It
is, in fact, a matrix constructed with the values of the spectra of the seismogram divided into different consecutive time
windows, generally superimposed. It can be conceived as a 3D visual representation of the matrix and can be understood as a
function of the frequency content (amplitude of the PSD's) over time. In this study we use the matrix of the values of the
PSD amplitudes (A (f, t)) obtained from the seismogram. Spectrograms are commonly used in different fields (noise, sound
180   (sonograms)....). The spectrum of a time series yields information of the distribution/content of frequencies in the signal, as a

whole, whereas in the spectrograms, this frequency content is presented distributed over time. A logarithmic scale for the amplitudes is used to facilitate the representation because of the wide range of amplitude values obtained along a whole signal. Although the image of the spectrogram provides information on the evolution of the frequency content in time, when considered the values of the matrix, a more detailed information is obtained. Another useful representation of the matrix of

185 the amplitudes of the PSD's is in a 3D (amplitude, frequency, time) plot (waterfall mode). Figure 1 shows, as an example, the two already mentioned representations of the evolution of the frequency content of a SON section time series (seismogram) (a), the spectrogram (b) and the waterfall (c). Moreover, details of PSD transect along frequency for specific time (10 s) (d), and for a specific frequency (9.3 Hz) along time in two different scales (e and f) are presented.

3.1 Interpretation of the shape of the SON section spectrogram.

190 A seismological description of the attenuation of the seismic waves with distance can be obtained in academic texts as those of Aki and Richard (1980), or Udías (1999, pages 253-263). More recently, Burtin et al., (2016) presented a simplified version of the content for a non-specialist audience. The purpose of the present section is to show the relationship between the parameters that allow generate a synthetic spectrogram through analytical equations and a spectrogram obtained from an observed seismogram and establish the dependencies between the variables involved.

195 As stated above, one distinctive feature of the SON section depicted in the spectrograms, corresponding to a gravitational mass movement approaching a sensor, is the increasing with time of the amplitude of the high frequencies in a pseudo-exponential shape. We assume that this increase is due to the properties of wave propagation in a medium, mainly the effect of the attenuation (anelastic/intrinsic and geometrical spreading (e.g., Lay and Wallace, 1995; Udías, 1999) of the seismic waves, and possible mass increasing by entrainment as it approaches the sensor (this is the case of snow avalanches). This

200 increasing pattern could be attributed to the Doppler effect. However, the quantification undertaken by Biescas (2004) rejected this because of the difference of two orders of magnitude between the speed of the avalanche ($\sim 10^1$ m s^{-1}) and that of the waves traveling across the ground ($\sim 10^3$ m s^{-1}). This can also be valid in the case of debris and lahars given the similar order of magnitude of their velocity values ($\sim 10^1$ m s^{-1}) with respect to those of seismic waves (e.g., Rickenmann, 1999; Vázquez et al., 2016).

205 To reproduce the mentioned shape of a spectrogram, and test our assumption, a synthetic spectrogram was created using the analytical Eq. (1) of the decay of the seismic amplitude with distance [e.g., Aki and Richards, 1980]. This equation estimates the wave amplitude A (t, f) at a point at a distance r' from a fixed-point source (r'=0) (Fig. 2) with a signal amplitude AS (fs, ts), function of given t_s (time) and f_s (frequency). This amplitude A (t, f) is a function of t (time) and f (frequency). In Eq. (1) the geometrical spreading and intrinsic attenuation are considered affecting at the frequency content, f.

210 $$A(t,f) = \frac{AS(f_s, t_s)}{(2\pi\, hr'(t'))^{1/2}}\ e^{-\alpha(f)r'(t)}\ ,$$ (1)

This is a decreasing function as distance r' increases from the source. Amplitude AS (f_s, t_s) is, in fact, the amplitude that a hypothetical sensor would measure at r' = 0. AS (f_s, t_s) can be considered to last a time interval. In our case, surface waves generated by the mass movement were considered in Eq. (1) following the studies on snow avalanches by Vilajosana et al., (2007b). This equation is obtained considering the energy flux of the seismic wave through a cylindrical surface of height h

215 and radius r'. The exponential term corresponds to the intrinsic attenuation where

$$\alpha(f) = \frac{\pi f}{Q(f)c(f)} \tag{2}$$

and h=k c(f)/f. Factor k is associated with the skin depth (Rukhadze and Shokri, 1997; Festa et al., 2005). Q(f) is the ground quality factor and c(f) the phase velocity of the surface waves.
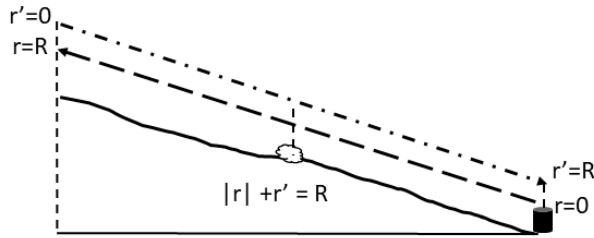
220 **Figure 2. Scheme of the double distance coordinates system. Origin situated at the sensor (r = 0), and origin at the source r'=0, being r(t) the distance of the source to the sensor and R= |r(t)| + |r'(t)|.**

Note that in Eq. (1) we are considering the time domain and not the frequency domain. This expression has been already used by other authors for purposes of localization using the amplitude of the seismic signals (e.g., Jolly et al., 2002; Kumagai et al., 2013; Pérez-Guillen, 2019).

225 Figure 3 shows, as an example, a detail of the effect of the attenuation (geometrical spreading and intrinsic attenuation) with distance to the source on the amplitude and frequency content of a time series using synthetic seismograms. The theoretical time series (Fig. 3a) is created by the function:

$$S(t) = \sum_1^8 n_i.\cos(2\pi f_i t) + BR(t) \tag{3}$$

With n_i = [5,10, 25, 30, 15, -15, 20, 30] units (u) and f_i= [1, 7,10,12,15, 20, 30, 40] Hz. BR(t) is an aleatory signal of 150 u of

230 maximum amplitude (not displayed). In Fig. 3 b de PSD of the theoretical function is shown. In figures 3c, e and g the time series and the corresponding PSD (Figs. 3d, f and h) are presented for different distances from the source: [500, 2000, 3000] m. The intrinsic attenuation factor Q (f) = 2.8 f 0.57 and the phase wave velocity c(f) = 8.9 f + 722 in m s^{-1} are considered as functions depending on frequency.

Earth **Surface**
Dynamics
Discussions

The terrain values used, Q(f) and c(f), correspond to those obtained in Vilajosana et al., (2007a) from one experiment carried

235   out at the Ryggfonn site. Note that in Fig. 3 higher frequencies are attenuated with distance, and that at 3000 m only 1 Hz is

observed in the time series (in this representation $(2\pi h)^{1/2}$ of Eq. (1) is assumed to be 1).
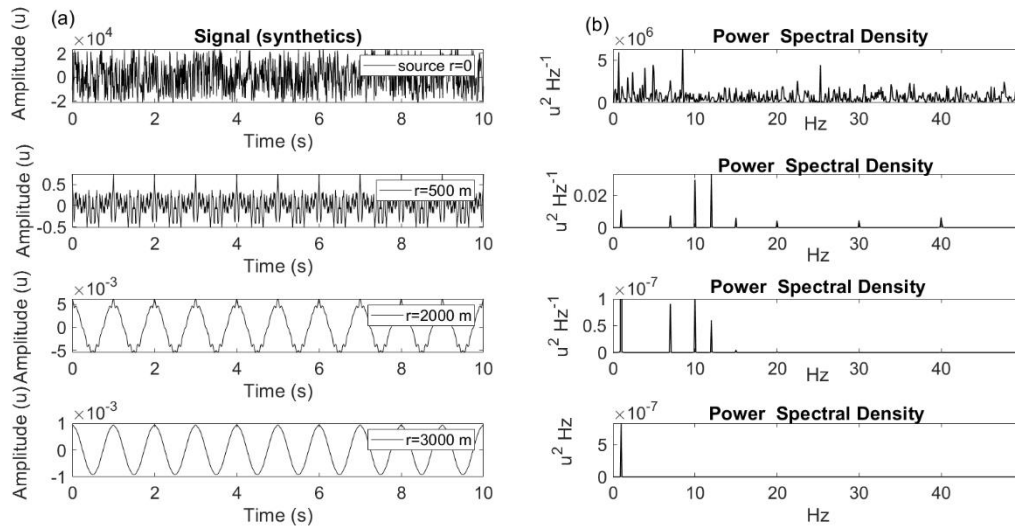
Figure 3. a) Synthetic time series generated by given frequencies (see text) calculated at different distances (r) from the source and

240   **b) their corresponding power spectral density (PSD). The power spectral density clearly shows the pics of specific frequencies.**

Amplitude scale in units.

Since our attention is focused on the signals recorded at the sensor, Eq. (1) can also be read as the variation of the amplitude

at the sensor as the source approaches it. We can then consider the source approaching the sensor according to r(t) (Fig. 2).

This implies a change of coordinates system, being r(t) the distance of the source to the sensor (i.e., r = 0 at the sensor) and

245   since R= |r(t)| + |r'(t)|, r'(t) can be expressed as |r'(t)| = R − |r(t)|. Note that as the point source approaches the sensor, r

becomes 0 and r'= R. Moreover, r increases in time because -R < r < 0 and the Eq. (1) becomes the increasing function (Eq.

(4)). Note that in this interval the exponential has its maximum at r = 0.

$$A(t,f) = \frac{AS(f_s, t_s)}{(2\pi h\ (R-|r(t)|))^{1/2}}\ e^{-\alpha(f)R}\ e^{\alpha(f)r(t)} \tag{4}$$

Assuming $v_m(t)$ the mass speed r(t) can be expressed as r(t) = $v_m(t)$ t and Eq. (4) can be expressed as

250    $$A(t,f) = K'(t,f)\ e^{\beta't}, \tag{5}$$

where

$$K'(t, f) = \frac{AS(f_s, t_s)\, e^{-\alpha(f)R}}{(2\pi\, h\, (R - |r(t)|))^{1/2}} \tag{6}$$

and

$$\beta' = \alpha(f)\, v_m(t) \ . \tag{7}$$

255   In these expressions we use β' instead of β'(t, f) for simplicity.

Equation (5), represents the variation of the amplitude in time and frequency, and is an increasing function in time, t. This increase depends on K'(t, f) which depends on the decreasing function on time $r(t)^{1/2}$, and on the exponential function of t modulated by β' which depends on the ground characteristics that are frequency dependent. The factor $e^{-\alpha(f)R}$ is a constant value of r and of t.

260   Realistically speaking, we would have to consider a source point at each r (t). However, in a first approximation, we only consider only one moving source point. Because of $v_m(t) \ll c(f)$, the travel time of the seismic waves can be assumed to be instantaneous. The final seismic energy recorded in the sensor would be the sum of all the contributions. However, owing to the seismic wave attenuation characteristics, the contributions to the sum of the farther sources would be smaller, than those nearer the sensor.
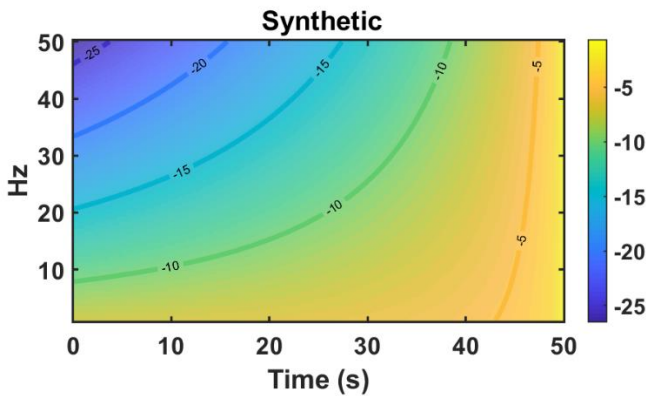
265

Figure 4. SON section synthetic spectrogram generated by Eq. (5). See text for the parameters used. Colors: amplitude in log10 scale.

The preceding relates the variation of the amplitude of the waves (seismograms) with the time (or distance). Since the square of the amplitude and the frequency content of a time series is preserved in its PSD, the amplitude variation of the signal over

270   time can be detected in the spectrograms.

Figure 4 shows, as an example, a synthetic spectrogram of a theoretical SON section using Eq. (5). In this case, a unitary impulse of amplitude ($AS(f_s, t_s) = 1$ u) is considered. The terrain values used, Q(f), and c(f), are those indicated above obtained by Vilajosana et al., (2007a). The velocity of the approaching mass to the sensor is assumed $v_m = 10$ m s^{-1} and factor k=0.25. Note the similarity in shape of this synthetic spectrogram with those of the SON sections obtained from the seismic signals (e.g., Fig. 1b). Therefore, we can consider that Eq. (5) can account for the shape of the SON sections of the spectrograms. The time increasing shape of the amplitudes of the frequencies in the SON section of the spectrogram is determined by the dependence on frequency of the exponential coefficient β' (Eq. 7). This is due to α (f) (Eq. 2), and not to r (t), which is not frequency dependent. The effect of r (t) on the spectrogram is an increase in the amplitude values for each frequency in the same ratio for each time not which does not affect the increasing shape. This would be the same effect with an increase in mass. Since α (f) is independent of the time and distance, its role in Eq. (7) is a constant of multiplication over time.

Table 1. Steps of spectrogram treatment (algorithm)

Spectrogram treatment (ST)
a) Enhancement of the spectrogram SON section
b) Creation of Bounded Matrix (image)
c) Conversion to Binary image
d) Edge detector mask Application
e) Iterative application of Hough transform (*determination of parameters of the line (q, r)* and *determination of the slope (a_i) and the (b_i) y-intercept*)
f) Computing the mean values *(a, b)*
g) Conversion to *b* and *K* values

Having established the relationship between a synthetic spectrogram and one generated from a seismogram, we are now interested in estimating the K' and β' values from a spectrogram of measured data.

4 Spectrogram treatment (ST).

The values of K' and β' of the SON section of a spectrogram will allow us to obtain information on the physical process of the mass movement since they are related mathematically to them (Eq. (5-7)). To this end, the spectrogram was analyzed as an image using the Hough Transform (HT) shape detection algorithm (Hough, 1962). The HT is a technique used to find shapes in a binary digital image. It allows to find all kind of shapes that can be expressed mathematically, for example lines or circles. In our case, we use the Linear Hough Transform algorithm that estimates the two parameters (a, b) that define a straight line in a search domain. Prior to the application of HT, the spectrogram must be prepared in a sequential procedure (ST) as a suitable image highlighting the contours to be determined (Table 1). To this end, we simulate the effect of the eye to determine the borders, that is, we determine a threshold limit (ratio) between amplitudes. To detect the borders, we fix an

295   amplitude threshold Ath. By imposing this condition on the implicit function (Eq. 5), the function F (t) (Eq. 8) for the amplitude A^{th} is obtained

$$F(t) = K'(t, f) \, e^{\beta'(t,f)t} \tag{8}$$

This function represents the variation of the frequency in time of a given amplitude value ($< A^{th}$).

Figures 5a to 5e show the steps carried out to obtain an image showing the outline of the shape. These figures show the
300   graphical representation of the values, although it is a numerical process. In Fig. 5a the matrix of amplitude values A (t, f) is presented as a spectrogram, b) The matrix is band-pass filter (in amplitudes) for all the times and complete set of frequencies. The values were split in two groups according to selected threshold values (A^{th}) to highlight the spectrogram SON section (Fig. 5b), c) The filtered matrix (bounded matrix image) was converted into a binarized (black and white) image to distinguish the arrivals corresponding to the most energetic frequencies (Fig. 5c). The method employed to obtain
305   this binary color image is known as "optimal thresholding", where white delimits the shape, and black corresponds to the background (Ridler and Calvard, 1978). d) The binary image was convolved with an edge detector mask (Ridler and Calvard, 1978) to reinforce the trace of the line of interest to obtain their geometrical parameters (Fig. 5d). e) The HT was iteratively applied to detect the different straight lines once the final edge detector-binary image is adequately prepared. Several lines were identified systematically by the HT algorithm to obtain the parameters a_i (slope) and b_i (f-intercept) in a
310   previously imposed coordinate system (t, f) (Fig. 5e). From these parameters, mean values (a, b) and their variance are obtained. Thus, the final equation for the shape of the spectrogram SON section is

$$f(t) = b + at \tag{9}$$
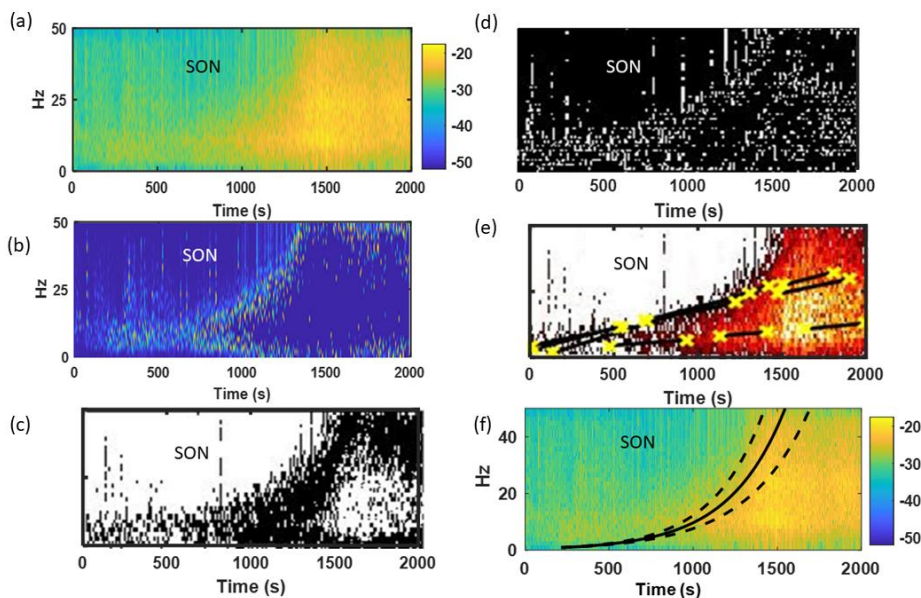
Figure 5. Images illustrating the steps of spectrogram treatment (ST): a) Original Spectrogram (colors: amplitudes in log₁₀ scale as in f). b) Bounded matrix image. SON section enhanced with threshold filtered amplitudes. c) Binary image (180 x 1465 pixels) of b). d) Edge detector-binary image. e) Straight lines obtained by the application of Hough Transform HT to image d) (slope (a_i) and the (b_i) y-intercept). f) Original Spectrogram image (a) with the exponential curve with the β' and K values obtained superimposed. Horizontal axes are time

A link between b and a (Eq. 9) and the coefficients $K'(t, f)$ and $\beta'(t, f)$ (Eq. (5)) is necessary. Note that Eq. (8) can be expressed as a linear equation by taking logarithms,

$$F'(t,f) = \ln K'(t,f) + \beta'(t,f)\, t \tag{10}$$

The comparison of the linear Eq. (9) and Eq. (10) gives us the y-intercept term of the linear equation $b = \ln K'(t,f)$ and the slope $a = \beta'(t,f)$. K' and β'' are dependent on time and frequency. Note that a and b are constant, but the mean values of those were obtained from the different adjustments in time. To assess this situation, an analysis of the dependence of the coefficients on frequency is first required. Remind that HT discriminates the amplitudes of the frequencies for each time using a selected threshold value (ratio) to determine the increasing shape of the SON section of the spectrogram with time (or distance). The dependence on frequency of $\beta'(t, f)$ (Eq. 7) is due to α(f), and not to r(t) ($r(t) = v_m(t)\, t$). The time dependence is due to the mass speed variation in time. The variation in r (t) will produce a similar variation in the amplitudes for each time. This comparison leads to a β' independent of frequency and time, which we call β. This result is not inconsistent since the value of the slope, a, is obtained from the average of the different slopes of the fits to the spectrogram image and it can be assumed as an approximation. The same effect causes $K'(t, f)$ (Eq. 6), whose dependence on f, depends on the frequency of the source in $AS(f_s, t_s)$. Note that the amplitude threshold between the frequencies is linked to $K'(t, f)$ at each time. Therefore, we can assume that K' is constant, called K, independent of the frequency.

After these considerations an approximation of Eq. (10) is

$$F'(t,f) = \ln K + \beta\, t \quad \text{or}$$

$$F(t,f) = K\, e^{\beta t} \tag{11}$$

Where K and β are the parameters that determine the increasing shape of the spectrogram. In Fig. 5f, the curve and margins calculated with Eq. (11) for a K and a β are overlapped on the spectrogram of Fig. 5a, as an example.

5 Application of the ST method to different signals generated by different gravitational mass flows. Results

5.1 Lahars

The lahars of the Colima Volcano were monitored by different instruments installed ~100 m away from of the Montegrande ravine (Fig. 6). The site and the data acquisition system are described in Vázquez et al., (2016). The data considered here were the subject of these contribution. In that paper the evolution of the frequency content of the seismic signals was used to

discern the different seismic sections connected with the different phases of the lahars (front, body, and tail). Spectrograms
345 and different frequency bands were analyzed to this end. Lahars occurred on 25 June and 15 September 2012, 11 June 2013
and 24 July 2013 are analyzed in this work. The activity of the volcano in the period was the purpose of Arámbula-Mendoza
et al., (2018). Characteristics of the 15 September 2012 lahar are described in Vázquez et al., (2014). The speeds of the
lahars ranged between 1.3 m s^{-1} and 3.6 m s^{-1} as deduced from video images (Vázquez, 2016). Table 2 shows the lahars
seismic signal durations that were of the order of half an hour. The larger one had a duration of around 5000 s (2013/07/24)

350
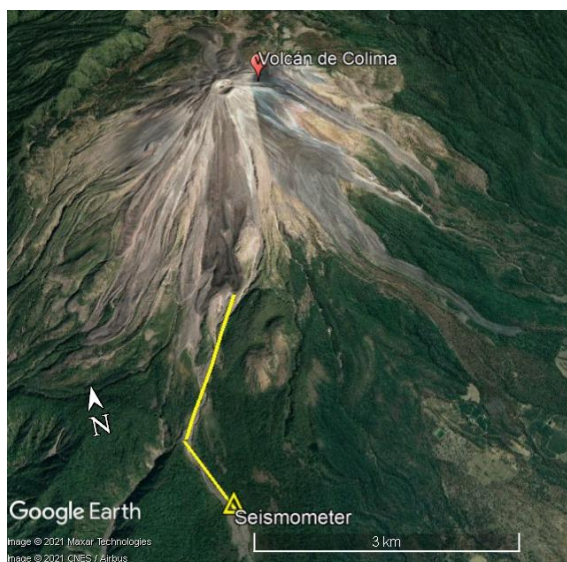
**Figure 6. © Google Earth image showing the Colima volcano (México). In yellow, the section of the Montealegre Ravine path where
the lahar seismic signals are originated. The seismometer position is indicated.**

Table 2. Information of the signals of the Colima Volcano studied lahars. Event: name of the lahar. Sig. Duration (s): Duration of
355 **the total signal in seconds. SON Duration (s): Duration of the SON section in seconds. SON/SIG: ratio between the values of the
previous columns. K(Hz) and β (s^{-1}) with standard error computed values. Last row: averaged values of the different rows.**

Event	Sig. Duration (s)	SON Duration (s)	SON/SIG	K(Hz)	β ± σ$_β$ (s^{-1})
20120625	3000	700	0.23	1.000	0.0040±0.0020
20120915	4500	1000	0.22	0.188	0.0035±0.0011
20130611	5000	800	0.16	1.749	0.0024±0.0006
20130724	5000	1500	0.30	0.920	0.0030±0.0003
Average	4375±1639	1000± 616	0.23±0.01	0.96±1.11	0.003±0.001

with a SON section of around 1500 s. The SON section is determined just before the SOB section. The SON sections in the studied lahars correspond to the 16% to 30% of the total duration of the signal (Table 2). Considering the duration of the SON sections the first signals of the lahars came from approx. 1950-2900 m from the sensor (Fig. 6). We consider that the transmission of the waves on the ground is instantaneous because of the speed of the seismic waves is three orders of magnitude higher than the events speed. Table 2 also shows the β and K values obtained using the presented method. Figure 7 shows the seismogram, spectrogram, and bounded matrix image of the first 2000 s of the 20130724 lahar with the curves F (t) (Eq. (11)) superimposed calculated with the β and K values indicated in Table 2.
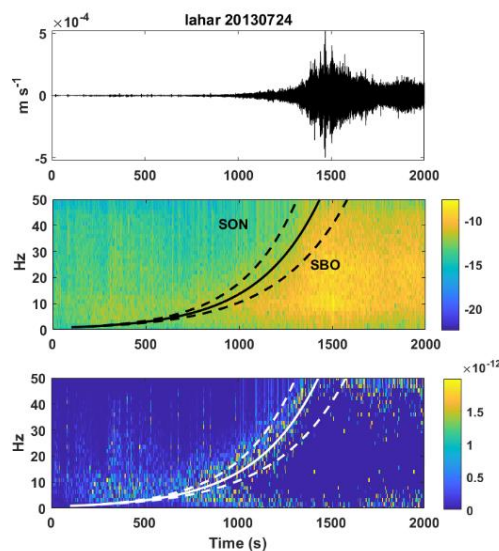
Figure 7. From top to bottom: vertical component seismogram, spectrogram and bounded matrix image of the spectrogram of lahar 20130724. Horizontal axes are time. Spectrogram amplitude in $\log_{10}$ in colored scale. Color scale of bounded matrix image amplitude in $(m\ s^{-1})^2$ s. Superimposed the exponential curves with the corresponding K and β values (Eq. 5) and the error margins (Table 2).

5.2 Debris flows

The data were obtained in the Lattenbach Torrent in the west Tyrol (Fig. 8). This torrent was monitored by different instruments. In Kogelnig et al., (2014) a description of the Lattenbach site and studied debris flow is presented. The maximum flow velocity of the studied event was 7 m s^{-1} (e.g., Kogelnig et al., 2014).

In Fig. 9 the time series, spectrogram, and bounded matrix image of the SON section of the geophone (right) and infrasound (left) signals of the debris flow are shown. Because the seismic data were recorded in a 10 Hz vertical geophone, unfortunately, no frequency below this value was obtained. However, the infrasound data contains the lower frequency content that allows us to detect better the increasing shape of the SON sections. In Table 3 the duration of the signals

recorded by the geophone and infrasound sensor are shown. The duration of the infrasound signals was of the order of an hour and the SON section corresponds to the 7% of the total duration. The corresponding values for the seismic data are not considered because of its inadequate quality.

390   Table 3 also indicates the values of β and K obtained from both type of data. The infrasound values were used to calculate the curves plotted on the spectrograms and bounded matrix image (Fig. 9). Note that the curves are also valid for the seismic data. This result confirms the existence of a coupling between infrasound and seismic data (Ichihara et al., 2012; Suriñach et al., 2018; Marchetti et al., 2020). The comparison between the time series and the spectrograms of the signals from both
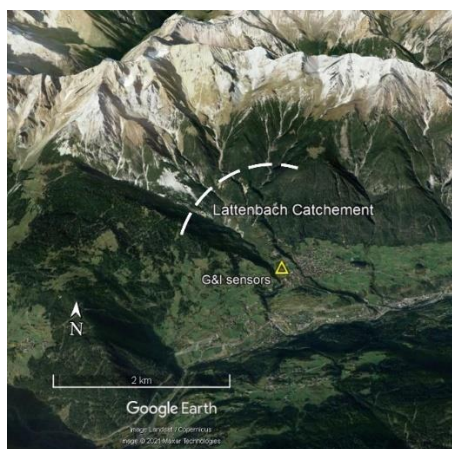
395   **Figure 8. © Google Earth image showing the Lattenbach Debris Flow catchment (Austria). In white, distance from where the debris flow seismic signals are originated; geophone and infrasound sensors location are indicated by a triangle.**

sensors (speed of the ground and variations in pressure) were carried out in Kogelnig et al., (2014) indicating an early detection of the infrasound with respect to the seismic. However, considering our previous comparison of the SON section of

400   the spectrograms, this result could be a consequence of the cutoff of the low frequencies of the geophone, because of the high sensor eigenvalue. The duration of the SON section indicates that the first signals of the debris flow came from approx. 1400 m from the sensor (Fig. 9). To obtain this value we considered that the speed of transmission of the infrasound in the air (approx. 340 m s-1), although it is not instantaneous, is three orders of magnitude higher than the events speed. This value agrees with the topographic features of the area.

405
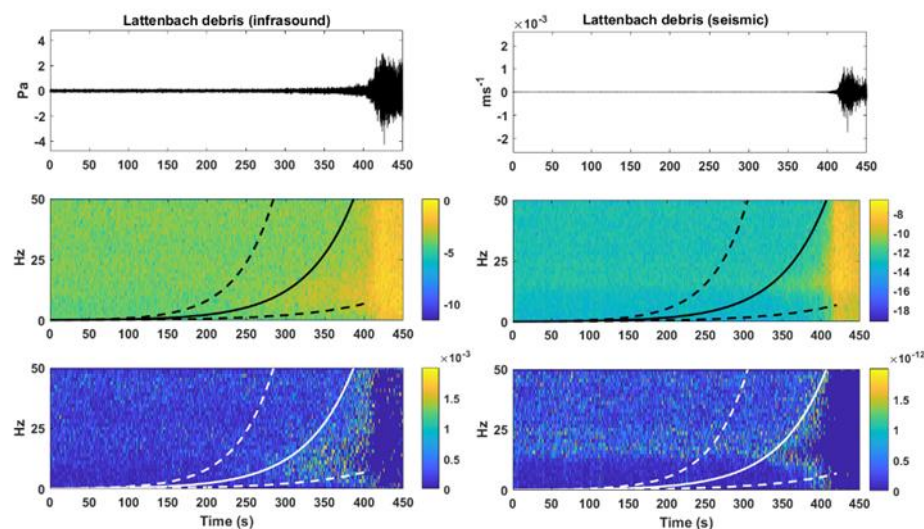
Figure 9. From top to bottom: vertical component seismogram, spectrogram, and bounded matrix image of the spectrogram of the infrasound (left) and seismic (right) data of the 01/09/2008 debris flow at Lattenbach catchment (Austria). Horizontal axes are time (s). Spectrogram amplitude in $\log_{10}$ in color scale. Color scale of bounded matrix image amplitude in $(m\ s^{-1})^2$ s for seismic data and in Pa^2 s for infrasound data. Superimposed the exponential curves with the corresponding K and β values (Eq. 5) and the error margins (Table 3).

Table 3. Information of the seismic and infrasound signals of the Lattenbach debris flows. Signals: type of measurement. Sig. Duration (s): Duration of the total signal in seconds. SON Duration (s): Duration of the SON section in seconds. SON/SIG: ratio between the values of the previous columns. K(Hz) and β (s^{-1}) with standard error: computed values.

Signals	Sig. Duration (s)	SON Duration (s)	SON/SIG	K(Hz)	$\beta \pm \sigma_\beta$ (s^{-1})
seismic	2000	78	0.04	1.01	0.01±0.01
Infrasound	3000	200	0.07	0.04	0.017± 0.005

5.3 Snow avalanches (VdLS and Ryggfonn)

Two sites are considered for this type of mass movement, the Vallée de la Sionne (VdLS) (Fig. 10) and the Ryggfonn (Fig. 12) experimental sites. Previously, in Suriñach et al., (2020) the β and K parameters of the SON sections of different type and size avalanches, recorded at two different sites (B and C) at VdLS were analyzed (Fig. 10). As a conclusion we obtained

that the avalanches can be grouped by similar β and K values according to their type: POW (powder snow), TRANS (transitional) and/or WET (wet snow). The description of each type of avalanches can be obtained in e.g., Pérez-Guillén et al., (2016) and references therein. Moreover, an evolution of the curves was observed associated to the evolution of the

425 avalanche along their path. Here, for the purposes of this paper only one avalanche of each type (TRANS, POW and WET, Table 4) recorded at site B are considered (Fig. 10). The avalanches front speeds at B that correspond to the SON section signals deduced from GEODAR measurements (Ash et al., 2010; Köhler, McElwaine et al., 2016; McElwaine, Köhler et al., 2017) were 38± 4 m s-1 for avalanche TRANS, 31 ± 3 m s^{-1} for POW and 26 ± 3 m s^{-1} for WET avalanche (Suriñach et al., 2020). Table 4 shows the durations of the avalanche signals and the β and K values obtained in Suriñach et al., (2020). The

430 durations of the signals do not exceed 3 minutes and the SON sections range between 14% and 50% of the total duration of the signals. Figure 11 shows as an example, the time series, spectrogram, and bounded matrix image of POW avalanche with the corresponding calculated curves with the values of Table 4. Considering the duration of the SON sections and the speed of the avalanche front, the first signals of the avalanche came from approx. 950 m (TRANS), 930 m (POW) and 780 m (WET) from the sensor. To obtain this result we consider that the transmission of the waves on the ground is instantaneous

435 because of the speed of the seismic waves is two orders of magnitude higher than the avalanches speed. These results are compatible with the 1200 m of distance from CB1 to B (Fig. 10). Note that the first signals of the wet avalanche start to be
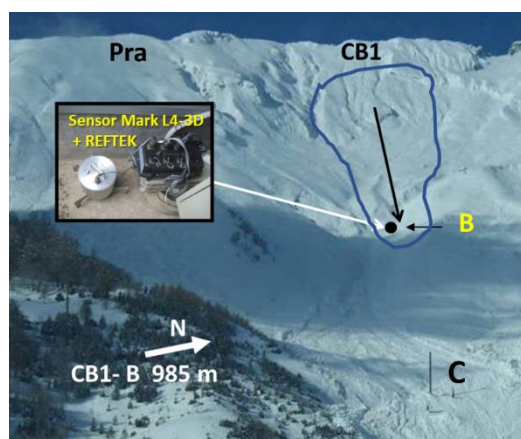
Figure 10. Locations B and C of the sensor at the VdLS test experimental site (Valais, Switzerland). CB1 and Pra avalanche
440 **release areas. Line and arrow: avalanche descending along path. inset: seismic station (Mark L-4C-3D sensor and Reftek–130 data acquisition system. Approximate distances: path length: 2600 m, Dh: 1205 m, CB1- B: 985 m,**

Earth **Surface**
Dynamics
Discussions
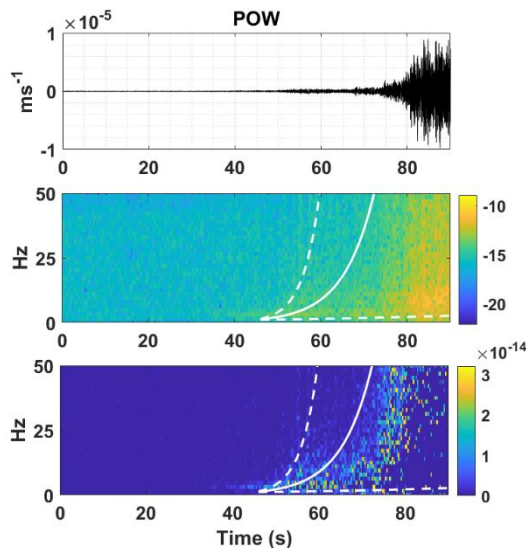
Figure 11. From top to bottom: FS seismogram, spectrogram, and bounded matrix image of the spectrogram of a Powder snow avalanche recorded in B at VdLS experimental site (SLF, Switzerland). Horizontal axis is time. Spectrogram amplitude in $\log_{10}$ in color scale. Color scale of bounded matrix image amplitude in $(m \ s^{-1})^2$ s. Superimposed the exponential curves with the corresponding K and β values (Eq. 5) and the error margins (Table 4).

Table 4. Information of the signals of snow avalanches recorded in B at VdLS experimental site. TRANS: transitional snow avalanche. POW: Powder snow avalanche. WET: Wet snow avalanche. They correspond to Av4 TRANS- L, Av5 POW-L and Av6 WET-M in Suriñach et al., (2020). Sig. Duration (s): Duration of the total signal in seconds. SON Duration (s): Duration of the SON section in seconds. SON/SIG: ratio between the values of the previous columns. K(Hz) and β (s^{-1}) with standard error computed values. Last row: averaged values of the different rows.

EVENT	Sig. Duration (s)	SON Duration (s)	SON/SIG	K(Hz)	$\beta \pm \sigma_\beta$ (s^{-1})
TRANS	180	25	0.14	3.10	0.10±0.07
POW	140	30	0.21	1.09	0.14±0.12
WET	60	30	0.50	3.32	0.05±0.02
Average	127±86	28±4	0.28±0.27	2.5±1.7	0.10±0.06

455   recorded at shorter distances than those of the POW and TRANS avalanches. This result agrees with the combination of the frequency content of the avalanches and the attenuation law of the seismic waves. Whereas the frequencies of wet

avalanches are in the range of 16 to 26 Hz and with a Cumulative Energy in % (CE (%)) equal to 0.7, the values of frequency for POW and TRANS are lower and in the range of 1.2 and 5 Hz with a CE (%) of 95.6 and 60, respectively (Pérez-Guillén et al., 2016). Considering that higher frequencies attenuate with distance more rapidly than lower frequencies,

460   wet avalanche signals will begin to be detected at distances closer to the sensor than other avalanche types.
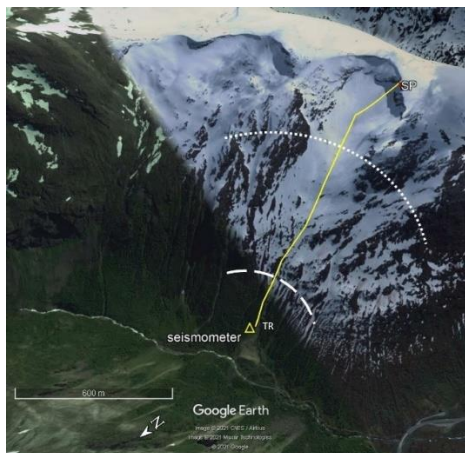
Figure 12. © Google Earth image showing the Ryggfonn experimental site (NGI, Norway). Avalanches path in yellow. In white approximate distances from where the avalanches seismic signals are originated. Dashed line d/d avalanches. Dotted line: d/m avalanches. Avalanches origin (SP) and seismmometer location in TR are indicated.

465   Four avalanches recorded at Ryggfonn experimental site (Norway, NGI) (Fig. 12) are also included in this study. Two avalanches of each type (dry-dense (d/d) and dry-mixed (d/m)) are considered (Table 5). These avalanches were used to determine the avalanche speed and the energy estimation from the seismic signals generated (Vilajosana et al., 2007a and Vilajosana et al., 2007b). Characteristics of the site can be found in these papers and references therein, and in Gauer and Kristensen (2016) and references therein. Averaged speeds for the front of the avalanches arriving to the sensor were 10 m s^{-1}

470   for d/d avalanches arriving to the sensor were 10 m s^{-1} for d/d avalanches and 25 m s^{-1} for d/m avalanches (Vilajosana et al., 2007b). The duration of the signals is of the order of 2 minutes, the d/d the shorter, and the SON section corresponds to the 37% of the total duration (Table 5). In Table 5 the obtained β and K values are shown. In Fig. 13 the time series, spectrogram, and bounded matrix image of the SON section of the dry/mixed avalanche 2004059 d/m are presented together with the corresponding curves. Considering the duration of the SON sections and the speed of the avalanche front, the first

475   signals of the avalanche came from approx. 1000 m distance for d/m and 300 m for d/d avalanches. To obtain this result we made the same consideration as for the case of the VDLS avalanches. These results agree with the length of the avalanche path (1608 m) and agree also with the fact that, due to their frequency content and waves attenuation law, avalanche d/d signals will begin to be recorded at distances closer to the sensor than those of m/d avalanches.

480   **Table 5. Information of the signals of the snow avalanches at Ryggfonn experimental site. Event: name of the event. d/m: dry mixed avalanche. d/d: dry dense avalanche. Sig. Duration (s): Duration of the total signal in seconds. SON Duration (s): Duration of the SON section in seconds. SON/SIG: ratio between the values of the previous columns. K(Hz) and β (s^{-1}) with standard error: computed values. Last row: average values of the different rows.**

Event	Sig. Duration (s)	SON Duration (s)	SON/SIG	K(Hz)	$\beta \pm \sigma_\beta$ (s^{-1})
2004059 d/m	80	40	0.5	0.37	0.91±0.05
2005106 d/d	120	35	0.3	1	0.23±0.11
2007081 d/d	150	30	0.2	0.78	0.14±0.20
2008113 d/m	95	45	0.5	0.04	0.08±0.04
Average	111±53	38±11	0.37±0.25	0.55±0.74	0.13±0.12

Figure 14 shows the topographic profiles of the path of the two sites (VdLS and Ryggfonn) for comparison. Note that VdLS
485   distance shot point (SP) to the sensor (B) is 1200 m, shorter than its equivalent distance at Ryggfonn, that is approx. 400 m longer. The averaged slope values are approximately the same, although the VdLS slope (ϕ_v = 31.5°) is slightly higher than that of Ryggfonn (ϕ_R =28.4°) value. The average duration of the avalanche signals of Ryggfonn are 111 ± 53 s with a SON/SIG 0.37 ± 0.25 s, whereas those of the three selected at VdLS are 127 ± 86 s and 0.42 ± 0.12, respectively. We consider these values of the same order, although the differences between the values of the different avalanche types are bear
490   in mind.
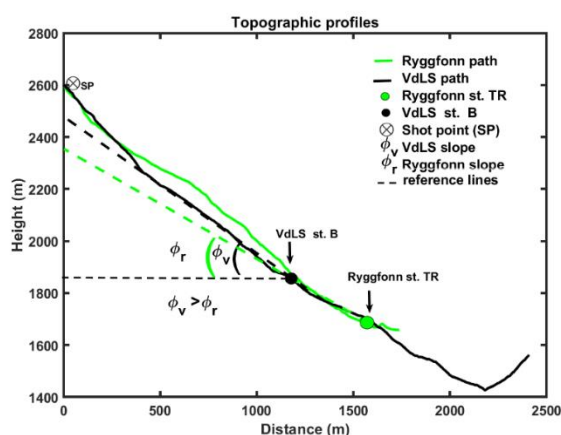
Figure 14. Topographic profiles of the path of the VdLS and Ryggfonn sites represented together for comparison. The distance from SP to sensor VdLS B is about 1200 m and from SP to for Ryggfonn sensor TR is approx. 1500 m. The path slopes near the sensors are ϕ_v =31.5° and ϕ_r = 26.4° for VdLS and Ryggfonn sites, respectively

495 **6 Discussion**

In Table 6 the average values obtained for each type of mass movement are presented. Note that the duration of the avalanche signals is much shorter (no more than 3 minutes) than that of the lahars and debris flow with a duration of the

Table 6. Summary of the averaged values of the information of the studied signals. EVENTS: Event type. SD± σ$_{SD}$ (s): Averaged
500 **duration of the total signal in seconds. SOND± σ$_{SOND}$ (s): Averaged SON section duration in seconds: SON/SIG ± σ: Averaged ratio**
between the values of the previous columns, and the average values of K and β with standard error.

EVENTS	SD ±σ$_{SD}$ (s)	SOND± σ$_{SOND}$ (s)	SON/SIG ± σ	K± σ$_K$ (Hz)	β ± σ$_β$ (s^{-1})
Lahars	4375±1639	1000± 616	0.23±0.01	0.96±1.1	0.003±0.001
Debris (I)	2000	200	0.10	0.039	0.017
Snow av. (RYGGFONN)	111±53	38±11	0.37±0.25	0.55±0.74	0.13±0.12
Snow av. (VDLS)	127±86	28±4	0.28±0.27	2.50±1.74	0.10±0.07

order of hours and half an hour, respectively. Regarding the duration of the SON section that of the avalanches is smaller than those of the debris and lahars in one and two orders of magnitude, respectively. The SON/SIG ratio, that of the debris
505 flow is smaller than the others, although we are conscious that we have only data of one event. As regards K and β, we have shown that, independently of the type of mass movement, it is possible to obtain these two parameters that characterize the increasing shape of the spectrogram SON section. The increasing, shape connected to a mass movement approaching a sensor, is described by these parameters according to the type of event (Table 6).

The average β value for lahars, around 0.003 s^{-1}, is two orders of magnitude lower than that of the avalanches (around 0.1 s^{-1}).
510 In between, are those of the debris flows, around 0.01 s^{-1}. The β value, the coefficient of the exponential (Eq. 11), is the responsible of the increasing shape. The effect of factor K is a shifting along the axes. As regards the average β values for avalanches, note that independently of the site (VdLS and Ryggfonn) these are similar. Considering the values obtained for lahars and debris, we can consider this assertion correct.
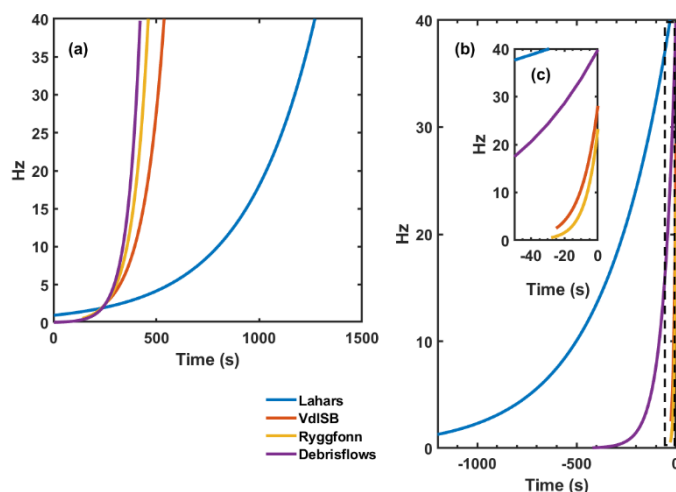
Figure 15. a) SON section curves obtained from the average K and β values (Eq. 5) of Table 6 for the different mass movements studied. b) The same curves with the origin of time at the sensor. c) Inset: detail of the 50 s prior to the avalanche reaching the sensor indicated in dashed lines in b).

In Fig. 15 the curves obtained with the average parameters of the events studied are presented simultaneously. To a better interpretation of these results, Fig. 15a shows the same curves but with the time zero corresponding when the mass movement is over the sensor, that is, time zero corresponding when the SBO section starts. The curves indicate that the appearance of high frequency seismic energy with time is faster in avalanches than in debris flow, being the slowest in lahars. In case of mass movement, the interval of time for its detection in a nearby sensor will be longer for lahars than for other mass movements, of the order of 1200 s in the first and 200 s or 20 s in the others (Fig. 15, Table 6). In other words, in the case of the occurrence of a lahar there will be more alert time than in the case of a snow avalanche.

We have shown that in the case of a specific gravitational mass movement, the different characteristics of each one of them are reflected in the shape of spectrogram (β and K parameters). This means that once the spectrograms of a type of event (snow avalanche, debris flow, or lahar) have been characterized, at a given location, the shape of the spectrogram can serve as an indicator of the characteristics of the event.
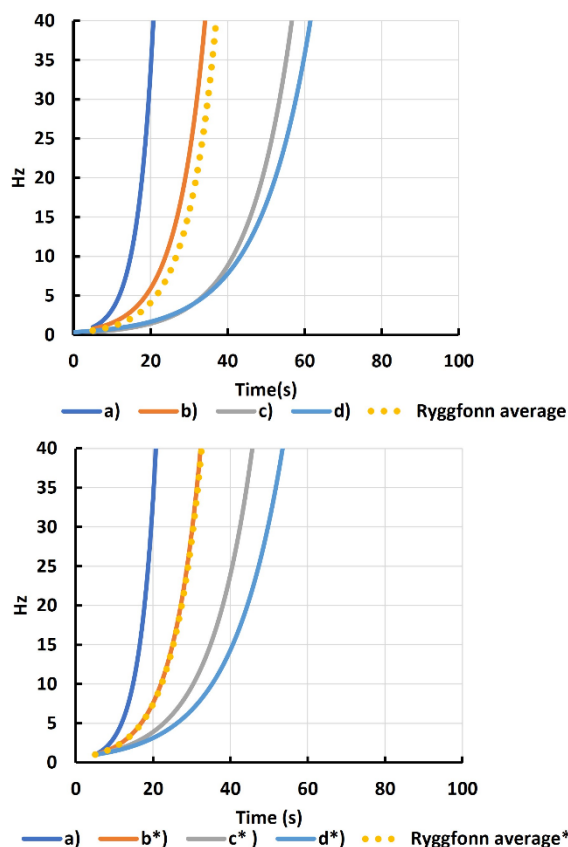
Figure 16. The role of parameter K (Hz). Top: Curves created using the K and β values (Eq. 5) for the snow avalanches at Ryggfonn. Values are indicated as (K, β). a) SA2005106 d/d (1, 0.23), b) SA2007081 d/d (0.78, 0.14), c) SA2004059 d/m (0.37, 091), d) SA2008113 d/m (0.04, 0.08), Ryggfonn average (0.55, 0.13) (Table 5) and bottom: (*) those created imposing K = 1 Hz. Note that the shape is the same.

7 The template

These results lead us to introduce a kind of template created with the parameters K and β that can help us characterize the type of events. However, to simplify the process, an explanation of the role of these parameters in this template is opportune. Previously, we had mention that the effect of K is a shifting along the axes. Figure 16-top shows the curves created using the
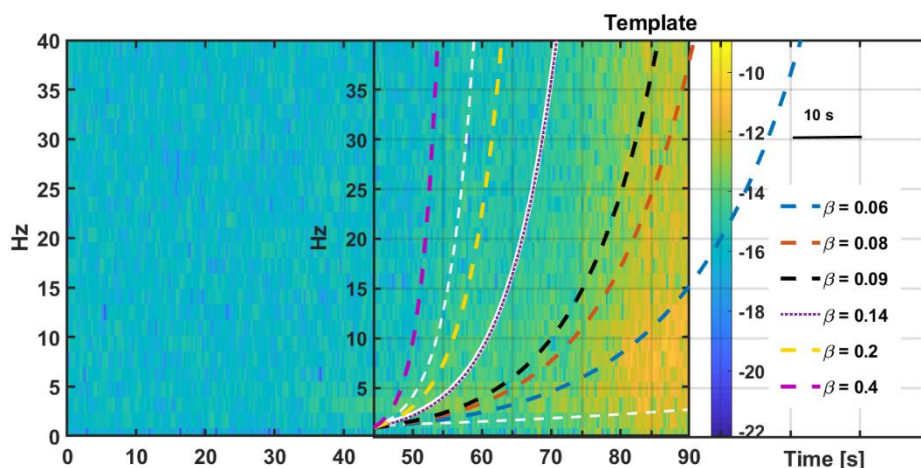
Figure 17. Example of use of the template created with different β values (K=1) (Eq. 5). Template superimposed to the avalanche POW spectrogram (Figure 11). Same scales of the template and spectrogram. Templated shifted along t axis to adjust by eye the best option. White lines correspond to the curves on Figure 11. Spectrogram amplitude in $\log_{10}$ in color scale.

values K and β for snow avalanches at Ryggfonn (Table 5) and Fig. 16-bottom those created imposing K =1 Hz. Note that the effect of K is a shift along the time axis. With the effect of K in mind, a template can be created for different values of β. Figure 17 shows, as an example, a template of curves created with different values of β (K =1 Hz) on the SON section spectrogram of avalanche POW (Fig. 11) recorded in sensor B at VDLS (Fig. 10). Note that the greater the beta, the stronger the increase in slope, or in other words, the faster the appearance of energy at high frequencies in the SON section. To obtain the β value of the observed spectrogram using the template, it is not necessary to develop all the ST process presented above. Once the template is established with the range of β values according to the type of mass movement and the specific site, comparison of the spectrogram with the template on the same scale can help classification within each type of mass movement. Figure 17 shows the comparison of the template with the spectrogram. The curve with a value of β =0.14 s^{-1} (in a dotted line) fits the shape of the spectrogram. This is just the value we obtained in the process previously presented. Figure 18 displays the spectrograms of the powder snow avalanche #17-3032 artificially released at VdLS. The release was in the Pra Roua area, placed to the left of CB1 (Fig. 10) and passed over sensors B and C (Roig-Lafon, 2021, page 132). The β values obtained for the data recorded at B and C using the template are 0.08-0.09 s^{-1} and 0.14 s^{-1} (in solid lines), respectively. Notice that these values are of the same order as those of the other VDLS avalanches. However, note the difference in the values, because of the evolution of the avalanche, larger in sensor C than in sensor B. Figure 19 shows the application of the template to the spectrogram of 20120915 lahar at Colima volcano as an example to obtain the β coefficient. Note that the order of magnitude of the β values of the template are different of those of snow avalanches.

However, the system of adjustment is the same as presented above. The value obtained for β is 0.0035-0.004 s^{-1}, similar of that obtained from the ST method (Table 2).
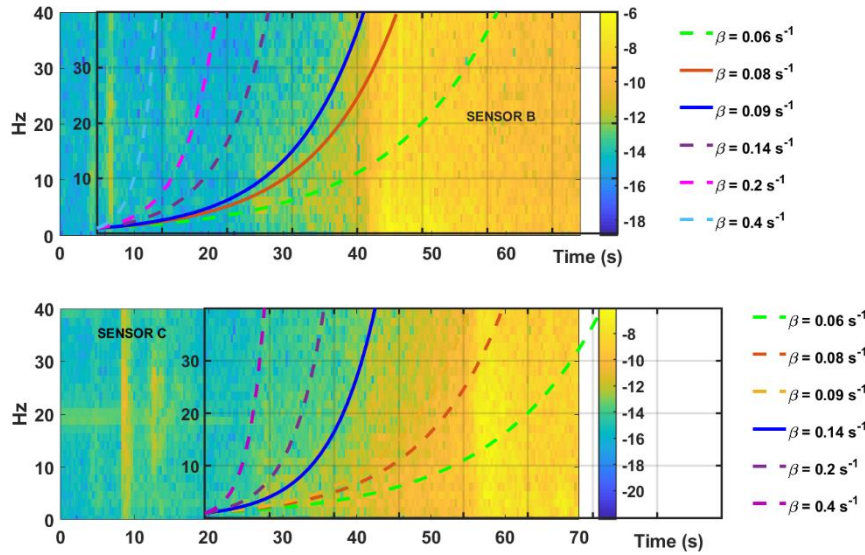
Figure 18. Determination of the β factor of the FS spectrograms at stations B and C (Fig. 10) of avalanche # 17-3032 artificially released in VdLS using the template. Spectrogram amplitude in log$_{10}$ in color scale. Solid lines: selected curves for the valid β value. Top: Sensor B, β = 0.08 – 0.09 s^{-1}. Bottom: Sensor C, β = 0.14 s^{-1}

8 Conclusions

We presented a methodology to obtain two parameters (K and β) that characterize the time increasing shape of the SON section of a spectrogram. This increasing shape is a consequence of the appearance of energy of high frequency in time as the gravitational mass approach the recorder sensor. This methodology includes a link between the seismic waves propagation properties and the results of the application of an image processing using the Hough transform.

We have obtained the K and β parameters for the SON section seismic signals generated by snow avalanches, lahars, and debris flows when they are approaching to a sensor. Differences in the order of magnitude of the values are obtained depending on the event type. The average β value for lahars is around 0.003 s^{-1}, that of the debris flows are one order of magnitude higher (0.017 s^{-1}), and one order of magnitude lower than that of the avalanches (0.12 s^{-1}). Furthermore, differences are observed in K and β for each type of event.

The parameters K and β allows us to construct curves that simulate the increasing shape of the spectrogram. The parameter β being the responsible of the increasing shape. We propose to use this fact to create a template with different values of parameter β to help in the classification within each type of mass movement.

580 The comparison of the spectrogram of an event with the appropriate template allow us to classify it. Note that this must be done for each site and for each gravitational mass movement. To this end, it is not necessary to reproduce all the ST process presented here, but only to superimpose graphically the corresponding spectrogram with the appropriate template at the same scale.

Once the β value determined, the characteristics of the mass movement must be fixed according to the criteria of experts.
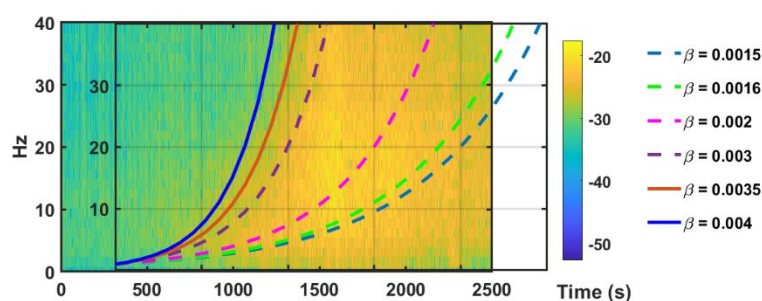
585

Figure 19. Determination of the factor β of the spectrogram of 20120915 lahar at Colima volcano (México) (Figure 6) using the template. Spectrogram amplitude in $\log_{10}$ in color scale. Solid lines: selected curves for the valid β value = 0.0035-0.004 s^{-1}.

Acknowledgements

This research was funded by the CHARMA (CGL2013–40828–R) and the PROMONTEC projects (CGL2017-84720-R) of
590 the Spanish Ministry of Economy, Industry and Competitiveness (MINEICO-FEDER). The authors wish to thank the UB avalanche Team for their assistance in the field campaigns. Special thanks are due to C. Pérez-Guillén and Pere Roig-Lafon for their contribution to the discussion on snow avalanches. The authors also wish to thank the SLF personnel, especially Betty Sovilla, for their help. Especially thanks to Rosario Vázquez and Lucia Capra (Instituto de Geofísica, UNAM) to make available the lahar seismic data. Johannes Hübl (BOKU) provide us the seismic and infrasound debris flow data. All other
595 data were obtained in field campaigns by the UB Avalanche Research Group. The authors acknowledge grants from the Instituto de Geofísica and Intercambio Académico, Coordinación de la Investigación Científica, UNAM, México. Codes were developed for our group, using MATLAB commercial package.

600 **References**

Abancó, C., Hürlimann, M., and Moya, J.: Analysis of the ground vibration generated by debris flows and other torrential processes at the Rebaixader monitoring site (Central Pyrenees, Spain), Nat. Hazards Earth Syst. Sci., 14(4), 929–943, doi:10.5194/nhess-14-929-2014, 2014.

Aki, K., and Richards, P. G.: Quantitative Seismology, vol. 1, WH Freeman and Company, San Francisco, 1980.

605 AlBinHassan, N.M., and Marfurt, K.: Fault detection using Hough transforms, SEG Technical Expanded Abstracts 22, 1719-1721, 2003.

Allstadt, K.: Extracting source characteristics and dynamics of the August 2010 Mount Meager landslide from broadband seismograms, J. Geophys. Res. Earth Surf., 118, 1472–1490, doi:10.1002/jgrf.20110, 2013.

Allstadt K., Matoza, R. S., Lockhart A. B., Moran, S. C., Caplan-Auerbach J., Haney M.M., Thelen, W. A., and Malone, S.D.:
610 Seismic and acoustic signatures of surficial mass movements at volcanoes, J. Volcanol. Geoth.Res., 364, 76–106, doi: 10.1016/j.jvolgeores.2018.09.007, 2018.

Almendros, J., Ibáñez, J.M., Alguacil, G., and Del Pezzo, E.: Array detection of a moving source, Seismol. Res. Lett. 73, 2 153-165, 2002.

Anderson, T. S., Moran, M. L., Ketcham, S. A., Lacombe, J.: Tracked vehicle simulations and seismic wavefield synthesis in
615 seismic sensor systems, Computing in Science & Engineering, 6 (6) 22 – 28, doi:10.1109/MCSE.2004.77, 2004.

Arámbula-Mendoza, R., Reyes-Dávila, G., Vargas-Bracamontes, D.M., González-Amezcua, M., Navarro-Ochoa, C., Martínez-Fierros, A., and Ramírez-Vázquez, A.: Seismic monitoring of effusive-explosive activity and large lava dome collapses during 2013–2015 at Volcán de Colima, Mexico, J. Volcanol. Geoth. Res., 351, 75–88, doi: 10.1016/j.jvolgeores.2017.12.017, 2018.

620 Arattano, M.: On the Use of Seismic Detectors as Monitoring and Warning Systems for Debris Flows, Nat. Hazards 20, 197–213, 1999.

Arattano, M., and L. Marchi, L.: Measurements of debris flow velocity through cross-correlation of instrumentation data, Nat. Hazards Earth Syst. Sci., 5, 137–142. SRef-ID: 1684-9981/nhess/2005-5-137, 2005.

Ash, M., Chetty, K., Brennan, P., McElwaine, and J., Keylock, C.: FMCW Radar Imaging of Avalanche-Like Snow
625 Movements, in Proceedings of the 2010 IEEE Radar Conference, Arlington, VA, USA, 10–14 May 2010, 102–107, 2010.

Biescas, B., Dufour, F., Furdada, G., Khazaradze, G., and Suriñach, E.: Frequency content evolution of snow avalanche seismic signals, Surv. Geophys., 24, 447–464, doi:10.1023/B: GEOP.0000006076.38174.31, 2003.

Biescas, B.: Aplicación de la sismología al estudio y detección de aludes de nieve. Ph. D. thesis, Universitat de Barcelona, http://hdl.handle.net/2445/34905 (access 25-01-2021), 130 pp., 2004.

630 Brodsky, E. E., Gordeev, E., and Kanamori, H.: Landslide basal friction as measured by seismic waves, J. Geophys. Res., 30 (24), 2236, doi:10.1029/2003GL018485., 2003.

Burtin, A., Hovius, N., and Turowski, J. M.: Seismic monitoring of torrential and fluvial processes, Earth Surf. Dynam., 4, 285–307, www.earth-surf-dynam.net/4/285/2016/, doi:10.5194/esurf-4-285-2016, 2016.

635 Caplan-Auerbach, J., and Huggel, Ch.: Precursory seismicity associated with frequent, large ice avalanches on Iliamna volcano, Alaska, USA, Journal of Glaciology, 53 (180), 128-140, doi:10.3189/172756507781833866, 2007.

Capra, L., Sulpizio, R., Márquez-Ramirez, V.H., Coviello, V., Doronzo, D. M., Arambula-Mendoza, R., and Cruz, S.: The anatomy of a pyroclastic density current: the 10 July 2015 event at Volcán de Colima (México), Bull. Volcanol, 80, 34, doi:10.1007/s00445-018-1206-4, 2018.

640 Cole, S. E., Cronin, S. J., Sherburn, S., and Manville, V.: Seismic signals of snow-slurry lahars in motion: 25 September 2007, Mt Ruapehu, New Zealand, Geophys. Res. Lett.   36 L09405, doi:10.1029/2009GL038030, 2009.

Coviello,V., Capra, L., Vázquez, R., and Márquez-Ramirez, V.H: Seismic characterization of hyperconcentrated flows in a volcanic environment, Earth Surf. Process. Landforms, 43, 2219–2231, doi:10.1002/esp.4387, 2018.

Coviello, V., Arattano, M., Comiti, F., Macconi, P., and Marchi, L.: Seismic characterization of debris flows: Insights into
645   energy radiation and implications for warning, Journal of Geophysical Research: Earth Surface, 124, 1440–1463, doi:10.1029/2018JF004683, 2019.

Dahlen, F.A.: Single-force representation of shallow landslide Sources, Bull. Seismol. Soc. Am., 83, (1), 130-143, 1993.

Dammeier, F, Guilhem, A., Moore, J. R, Haslinger, F., and Loew, S: Moment Tensor Analysis of Rockslide Seismic Signals, Bull. Seismol. Soc. Am., 105, (6), 3001–3014, doi:10.1785/0120150094, 2015.

650 Dammeier, F., Moore, J. R., Hammer, C., Haslinger, F., and Loew, S.: Automatic detection of alpine rockslides in continuous seismic data using hidden Markov models, J. Geophys. Res. Earth Surf., 121, 351–371, doi:10.1002/ 2015JF003647, 2016.

Deparis, J., Jongmans, D., Cotton, F., Baillet, L., Thouvenot, F., and Hantz, D.: Analysis of Rock-Fall and Rock-Fall Avalanche Seismograms in the French Alps, Bull. Seismol. Soc. Am., 98, (4), 1781–1796, doi:10.1785/0120070082, 2008.

Dietze, M., Mohadjer, S., Turowski, J. M., Ehlers, T.A., and Hovius, N.: Validity, precision and limitations of seismic rockfall
655   monitoring. Earth Surf. Dynam. Discuss., doi:10.5194/esurf-2017-12, 2017.

Doi, I., and Maeda, T.: Landslide Characteristics Revealed by High-Frequency Seismic Waves from the 2017 Landslide in Central Japan, Seismol. Res. Lett., 91 (5), 2719–2729, doi:10.1785/ 0220200032, 2020.

Favreau, P., Mangeney, A., Lucas, A., Crosta, G., and Bouchut, F.: Numerical modeling of landquakes, Geophys. Res. Lett. 37, L15305, doi:10.1029/2010GL043512, 2010.

660 Feng, Z., Lo, CM., and Lin, QF.: The characteristics of the seismic signals induced by landslides using a coupling of discrete element and finite difference methods, Landslides, 14, 661–674, doi:10.1007/s10346-016-0714-6, 2017.

Festa, G., Delavaud, E., and Vilotte, J.-P.: Interaction between surface waves and absorbing boundaries for wave propagation in geological basins: 2D numerical simulations, Geophys. Res. Lett. 32, L20306, doi:10.1029/2005GL024091, 2005.

Fuchs, F., Bokelmann, G., and the AlpArray Working Group: Equidistant Spectral Lines in Train Vibrations, Seismol. Res.
665   Lett. 89, 56-66, doi:10.1785/0220170092, 2018.

Gauer, P. and Kristensen, K.: Four decades of observations from NGI's full-scale avalanche test site Ryggfonn—Summary of experimental results, Cold Reg. Sci. Tech., 125,162–176, doi:10.1016/j.coldregions.2016.02.009, 2016.

Hibert, C., Mangeney, A., Grandjean, G., and Shapiro, N. M.: Slope instabilities in Dolomieu crater, Réunion Island: From seismic signals to rockfall characteristics, J. Geophys. Res., 116, F04032, doi:10.1029/2011JF002038, 2011.

670 Hibert, C., Stark, C. P., and G. Ekström, G.: Dynamics of the Oso-Steelhead landslide from broadband seismic analysis, Nat. Hazards Earth Syst. Sci., 15, 1265–1273, www.nat-hazards-earth-syst-sci.net/15/1265/2015/, doi:10.5194/nhess-15-1265-2015, 2015.

Hibert, C., Malet, J.-P., Bourrier, F., Provost, F. Berger, F., Bornemann, P., Tardif, P., and Mermin, E.: Single-block rockfall dynamics inferred from seismic signal analysis, Earth Surf. Dynam., 5, 283-292, doi:10.5194/esurf-5-283-2017, 2017.

675 Hough, P.V.C.: Method and means for recognizing complex patterns. US Patent 3069654. Washington, DC, Patent and Trademark Office, 1962.

Huang, C.-J., Yin, H.-Y., Chen, C.-Y., Yeh, C.-H., and Wang, C.-L.: Ground vibrations produced by rock motions and debris flows, J. Geophys. Res., 112, F02014, doi:10.1029/2005JF000437, 2007.

Ichihara, M., Takeo, M., Yokoo, A., Oikawa, J., and Ohminato T.: Monitoring volcanic activity using correlation patterns

680 between infrasound and ground motion, Geophys. Res. Lett., 39, L04304, doi:10.1029/2011GL050542, 2012.

Jolly A.D., Thompson, G., and Norton, G.E.: Locating pyroclastic flows on Soufriere Hills Volcano, Montserrat, West Indies, using amplitude signals from high dynamic range instruments, J. Volcan. Geotherm. Res., 118, 299 – 317, 2002.

Ketcham, S., Moran, M., Lacombe, J., Greenfield, R., and Anderson, T.S.: Seismic Source Model for Moving Vehicles, IEEE Transactions on Geoscience and Remote Sensing, 43, (2) 248 – 256, doi:10.1109/TGRS.2004.842212, 2005.

685 Kishimura, K., and Izumi, K.: Seismic Signals Induced by Snow Avalanche Flow, Nat. Hazards, 15, 89–100, doi-org.sire.ub.edu/10.1023/A:1007934815584, 1997.

Kogelnig, A., Hübl, J., Suriñach, E., Vilajosana, I., and McArdell, B.M.: Infrasound produced by debris flow: propagation and frequency content evolution, Nat. Hazards, 70, 1713–1733, doi:10.1007/s11069-011-9741-8, 2014.

Köhler, A., McElwaine, J.N., Sovilla, B., Ash, M., and Brennan, P.V.: The dynamics of surges in the 3 February 2015

690 avalanches in Vallée de la Sionne. J. Geophys. Res. Earth Surf., 121, 2192–2210, doi:10.1002/2016JF003887, 2016.

Konstantinou, K. I., Rahmalia, D.A., Nurfitriana, I., and Ichihara, M.: Fast Identification of Volcanic Tremor and Lahar Signals during the 2009 Redoubt Eruption Using Permutation Entropy and Supervised Machine Learning, Seismol. Res. Lett. 93 (1), 435–443, doi:10.1785/0220210176, 2022.

Kuehnert, J., Mangeney, A., Capdeville, Y., Métaxian, J. P., Bonilla, L. F., and Stutzmann, E., Chaljub, E., Boissier, P.,

695 Brunet,C., Kowalski, P., Lauret, F., Hibert,C.: Simulation of topography effects on rockfall-generated seismic signals: Application to Piton de la Fournaise volcano. . J. Geophys. Res.: Solid Earth, 125, e2020JB019874, doi:10.1029/2020JB019874, 2020.

Kumagai, H., Lacson, R., Maeda, Y., Figueroa, M. S., Yamashina, T., Ruiz, M., Palacios, P., Ortiz, H., and Yepes, H.: Source amplitudes of volcano-seismic signals determined by the amplitude source location method as a quantitative measure of event size, J. Volcanol. Geoth. Res., 257, 57–71, doi: 10.1016/j.jvolgeores.2013.03.002, 2013.

Lacroix, P., and Helmstetter, A.: Location of Seismic Signals Associated with Microearthquakes and Rockfalls on the Séchilienne Landslide, French Alps, Bull. Seismol. Soc. Am., 101(1), 341–353, doi:10.1785/0120100110, 2011.

Lacroix, P., Grasso, J.-R., Roulle, J., Giraud, G., Goetz, D., Morin, S., and Helmstetter, A.: Monitoring of snow avalanches using a seismic array: Location, speed estimation, and relationships to meteorological variables, J. Geophys. Res., 117, F01034, doi:10.1029/2011JF002106, 2012.

Lavoué, F., Coutant, O., Boué, P., Pinzon-Rincon, L., Brenguier, F., Brossier, R., Dales P., Rezaeifar, M., and Bean C. J.: Understanding Seismic Waves Generated by Train Traffic via Modeling: Implications for Seismic Imaging and Monitoring, Seism. Res. Lett., 92 (1), 287–300. doi:10.1785/0220200133, 2021.

Lay T., and. Wallace, T.C: Modern Global Seismology. Academic Press, Inc., ISBN: 9780080536712, 1995.

Leprettre, B. J., Navarre, J.-P, and Taillefer, A.: First results from a preoperational system for automatic detection and recognition of seismic signals associated with avalanches, J. Glaciology, 42, (141), 352- 363, 1996.

Lin, C. H., Kumagai, H., Ando, M., and Shin, T.C.: Detection of landslides and submarine slumps using broadband seismic networks, Geophys. Res. Lett. 37, L22309, doi:10.1029/2010GL044685, 2010.

Manconi, A., Picozzi, M., Coviello, V., De Santis, F., and Elia, L.: Real-time detection, location, and characterization of rockslides using broadband regional seismic networks, Geophys. Res. Lett., 43, 6960–6967, doi:10.1002/grl.54655, 2016.

McElwaine*, J. N., Köhler*, A., Sovilla, B., Ash, M., and Brennan, P. V.: GEODAR data of snow avalanches at Vallée de la Sionne: Seasons 2010-2015[Data set], Zenodo, doi:10.5281/zenodo.1042108, *equally contributing authors, 2017.

Marchetti, E., van Herwijnen, A., Christen, M. Silengo, M.C. and Barfucci, G.: Seismo-acoustic energy partitioning of a powder snow avalanche Earth Surf. Dynam., 8, 399–411, doi:10.5194/esurf-8-399-2020, 2020.

Moore, J. R., Pankow, K. L., Ford, S. R., Koper, K. D., Hale, J. M., Aaron, J., and Larsen, C. F.: Dynamics of the Bingham Canyon rock avalanches (Utah, USA) resolved from topographic, seismic, and infrasound data, J. Geophys. Res. Earth Surf., 122, 615–640, doi:10.1002/2016JF004036, 2017.

Moran, M. L., and Greenfield, R. J.: Estimation of the Acoustic-to-Seismic Coupling Ratio Using a Moving Vehicle Source, IEEE Transactions on Geoscience and Remote Sensing, 46(7), 2038 – 2043, doi:10.1109/TGRS.2007.910712, 2008.

Okal, E. A: On the possibility of seismic recording of meteotsunamis, Nat. Hazards, 106, 1125–1147, doi:10.1007/s11069-020-04146-x., 2021.

Pérez-Guillén, C., Sovilla, B., Suriñach, E., Tapia, M., Köhler, A.: Deducing avalanche size and flow regimes from seismic measurements. Cold Reg. Sci. Tech. 121, 25-41, doi: 10.1016/j.coldregions.2015.10.004, 2016.

Pérez-Guillén, C., Tsunematsu, K., Nishimura, K., and Issler, D.: Seismic location and tracking of snow avalanches and slush flows on Mt. Fuji, Japan. Earth Surf. Dynam., 7, 989–1007, doi:10.5194/esurf-7-989-2019, 2019.

Ridler, T.W., and Calvard, S.: Picture thresholding using an iterative selection method. IEEE Transactions on Systems, Man and Cybernetics, 8, 630-632, doi:10.1109/TSMC.1978.4310039, 1978.

Rickenmann, D.: Empirical relationships for debris flows. Nat. Hazards, 19(1), 47–77, doi:10.1023/A:1008064220727, 1999.

Rivera-Ríos, A. M., and Flores-Márquez, E. L.: Image-radargram analysis based on generalized Hough transform:
735 experimental cases, J. Geophys. Eng. 9, 558-568, doi:10.1088/1742-2132/9/5/558, 2012.

Roig-Lafon, P.: Identification of snow avalanche release areas and flow characterization based on seismic data studies. Ph.D. thesis University of Barcelona, http://diposit.ub.edu/dspace/handle/2445/180200, 170 pp., 2021.

Rukhadze, A. A., and Shokri, B.: Surface waves in thin layers of conducting media in the frequency range for the skin effect, Tech. Phys., 42 (12), 1446-1448, doi:10.1134/1.1258897,1997.

740 Saló, L., Corominas, J., Lantada, N., Matas, G., Prades, A., and Ruiz-Carulla, R.: Seismic energy analysis as generated by impact and fragmentation of single-block experimental rockfalls. J. Geophys. Res.: Earth Surf. 123, doi:10.1029/2017JF004374, 2018.

Schimmel, A., and Hübl, J.: Automatic detection of debris flows and debris floods based on a combination of infrasound and seismic Signals, Landslides, 13(5), 1181–1196, doi:10.1007/s10346-015-0640-z, 2015.

745 Schneider, D., Bartelt, P., Caplan-Auerbach, J., Christen, M., Huggel, Ch., and McArdell, B.W.: Insights into rock-ice avalanche dynamics by combined analysis of seismic recordings and a numerical avalanche model, J. Geophys. Res. 115, F04026, doi:10.1029/2010JF001734, 2010.

Sovilla, B., McElwaine, J. N., Steinkogler, W., Hiller, M., Dufour, F., Suriñach, E., Pérez-Guillén, C., Fischer, J –T, Thibert, E., and Baroudi, D.: The full-scale avalanche dynamics test site Vallée de la Sionne, In: International Snow Science
750 Workshop. Grenoble- Chamonix Mont Blanc October 07-11 2013, 1350 – 1357, 2013.

Spillmann, T., Maurer, H., Green, A.G., Heincke, B., Willenberg, H., and Husen, S.: Microseismic investigation of an unstable mountain slope in the Swiss Alps, J. Geophys. Res. 112, B07301, doi:10.1029/2006JB004723, 2007.

Suriñach, E., Sabot, F., Furdada, G., and Vilaplana, J.M.: Study of seismic signals of artificially released snow avalanches for monitoring purposes, Phys. Chem. Earth (B), 25 (9), 721-727, 2000.

755 Suriñach, E., Furdada, G., Sabot, F., Biescas, B., and Vilaplana, J.M.: On the characterisation of seismic signals generated by snow avalanches for monitoring purposes, Annals of Glaciology 32, 268-274, doi:10.3189/172756401781819634, 2001.

Suriñach, E., Vilajosana, I., Khazaradze, G., Biescas, B., Furdada, G., and Vilaplana, J. M.: Seismic detection and characterization of landslides and other mass movements. Nat. Hazards Earth Syst. Sci., 5, 791-798, doi:10.5194/nhess-5-791-2005, 2005.

760 Suriñach, E., Tapia, M., Roig, P., and Blach, X.: On the effect of the ground seismic characteristics in the estimation of mass movements based on seismic observation. Geophys. Res. Abstracts, EGU General Assembly 2018,20, https://meetingorganizer.copernicus.org/EGU2018/EGU2018-8479.pdf, https://www.researchgate.net/publication/331284120, 2018.

Suriñach, E., Flores-Márquez E.L, Roig-Lafon, P., Furdada, G., and Tapia, M.: Estimation of Avalanche Development and Frontal Velocities Based on the Spectrogram of the Seismic Signals Generated at the Vallée de la Sionne Test Site, Geosciences, 10, 113; doi:10.3390/geosciences10030113, 2020.

Udías, A.: Principles of Seismology, Cambridge University Press, 253-263, 1999.

van Herwijnen, A., and Schweizer, J.: Seismic sensor array for monitoring an avalanche start zone: design, deployment and preliminary results, J. Glaciology, 57 (202), 267-276, doi:10.3189/002214311796405933, 2011a.

van Herwijnen, A., and Schweizer, J.: Monitoring avalanche activity using a seismic sensor, Cold. Sci. Tech., 69 (2-3), 165-176, doi: 10.1016/j.coldregions.2011.06.008, 2011b.

van Ginkel, M., Hendriks, C.L.L., and van Vliet, L.J.: A short introduction to the Radon and Hough transforms and how they relate to each other, Quantitative Imaging Group Technical Report Series QI-2004-01, Netherlands, Delft University of Technology, 2004.

Varun R., Kini, Y.V., Manikantan, K., and Ramachandran, S.: Face Recognition using Hough Transform based Feature Extraction. Procedia Computer Science 46, 1491 – 1500, doi: 10.1016/j.procs.2015.02.069, 2015.

Vázquez, R., Capra, L., Caballero-García, L., Arambula, R., and Reyes-Dávila, G.: The anatomy of a lahar: deciphering the 15th September 2012 lahar at Volcán de Colima, Mexico. J. Volcanol. Geotherm. Res., 272,126–136, 2014.

Vázquez, R.: Estudio de la dinámica de lahares con base en el monitoreo de eventos en el Volcán de Colima: estimación de parámetros para el desarrollo de un sistema de alerta temprana. Ph.D. thesis, Universidad de Juriquilla, UNAM. https://repositorio.unam.mx/, 82 pp. 2016.

Vázquez, R., Suriñach, E., Capra, L., Arámbula-Mendoza, R., and Reyes-Dávila, G.: Seismic characterisation of lahars at Volcán de Colima, Mexico, Bull. Volcanol. 78 (8), doi:10.1007/s00445-016-1004-9, 2016.

Vilajosana, I., Suriñach, E., Khazaradze, G., and Gauer, P.: Snow avalanche energy estimation from seismic signal analysis, Cold Reg. Sci. Tech. 50, 72–85, doi: 10.1016/j.coldregions.2007.03.007, 2007a.

Vilajosana I., Khazaradze, G., Suriñach, E., Lied, E., and Kristensen, K.: Snow avalanche speed determination using seismic methods, Cold Reg. Sci. Tech. 49, 2-10, doi: 10.1016/j.coldregions.2006.09.007, 2007b.

Vilajosana, I.: Seismic detection and characterization of snow avalanches and other mass movements. Ph.D. thesis, Universitat de Barcelona, Facultat de Geología. Barcelona, 142 pp., 2018.

Walter, F., Burtin, A., McArdell, B.W., Hovius, N., Weder, B., and M. Turowski, J.: Testing seismic amplitude source location for fast debris-flow detection at Illgraben, Switzerland, Nat. Hazards Earth Syst. Sci., 17, 939–955, doi:10.5194/nhess-17-939-2017, 2017.

Zimmer, V.L., and Sitar, N.: Detection and location of rock falls using seismic and infrasound sensors, Engineering Geology 193, 49–60, doi: 10.1016/j.enggeo.2015.04.007, 2015.

Zimmer, V.L., Collins, B. D., Stock, G. M., and Sitar, N.: Rock fall dynamics and deposition: an integrated analysis of the 2009 Ahwiyah Point rock fall, Yosemite National Park, USA, Earth Surf. Process. Landf. 37 (6), 680–691, doi:10.1002/esp.3206, 2012.

Zobin V.M., Plasencia, I., Reyes, G., and Navarro, C.: The characteristics of seismic signals produced by lahars and pyroclastic flows: Volcán de Colima, México, J. Volcanol. Geoth. Res., 179 157–167, doi: 10.1016/j.jvolgeores.2017.12.012, 2009.